of the pitot tube. All pressures, including those on the static bench were measured relative to atmospheric pressure by means of a manometer with a resolution of 0.05 kPa. Details of the array locations are presented in Fig. 2. Tests were carried out with the five flow distortion configurations shown in Fig. 2.

Results

The flow angularities measured on the Turmo IVB engine for a distortion of 11.59% are presented in Table 1 against the nondimensional probe depth. It may be seen from the results that for this case the flow angularities were small with a maximum swirl angle of 2.0 deg. This indicated that the readings of the total and static pressure were not affected by the flow angularity. It also indicated that large angular accelerations of the air did not occur.

The small flow angularities downstream of the distortion generator were further evidenced by the data presented in Fig. 2, where it may be seen that the angular positions at which low total pressures occur, correspond to the locations of the areas of blockage of the distortion generator. Where insufficient data points were available to clearly indicate the effects of the flow distorters, the graphs are left blank.

The variations of the static and total pressure distributions at the inlet plane to the Turmo IVB gas turbine are presented in Fig. 2. As may be seen from Fig. 2, the distortions strongly affect the total pressure and have negligible effect on the static pressure. From the data obtained, the static pressure is virtually constant around the inlet up to DC(60) values of 24.1%, which is substantial for most engines. The variation of power measured for the Turmo IVB engine with DC(60) index is presented in Fig. 3.

As may be seen from Fig. 3, the effect of the flow distorters was to decrease engine power by about 3.7% over the range of distortions tested. Because the engine power is proportional to the mass flow through the engine, it is reasonable to assume that the mass flow through the engine was almost constant for all the tests, irrespective of the large variation in the DC(60) index.

Table 1 Flow swirl angle at engine entrance plane for DC(60) = 11.59%

Array point	Depth x/D, %	Angular location, deg		
		0	60	120
R1	3.22	0.5	−1.0	0.0
R2	13.6	0.0	−1.5	0.0
R3	32.3	0.0	−2.0	0.0
R3	68.1	0.0	1.5	−0.5
R2	86.7	0.0	0.0	−0.5
R1	97.1	0.0	0.0	−1.0

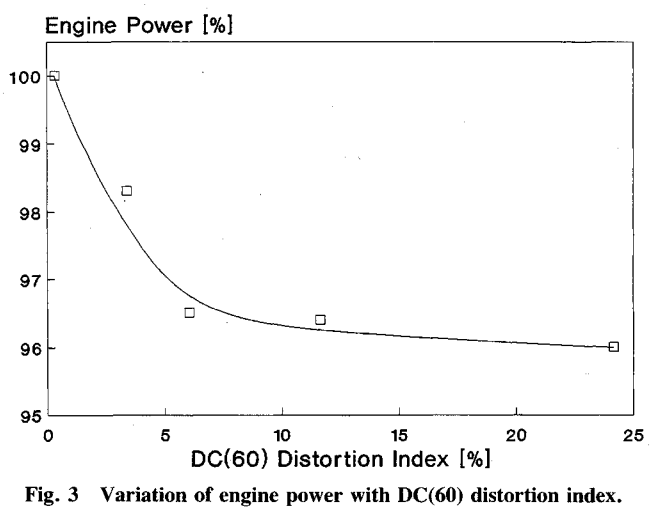

Fig. 3 Variation of engine power with DC(60) distortion index.

Conclusions

1) The primary variation of the flow in an engine inlet of the type of gas turbine tested resulting from flow distortions is of the dynamic pressure with variations of the static pressure being small.

2) The swirl resulting purely from flow distortions is small for the engine tested. This is consistent with the minimal static pressure variations in the angular direction that would otherwise be associated with large angular accelerations of the flow.

3) As was found by Reid,[2] the mass flow through the gas turbine does not vary to a large extent, irrespective of the comparatively large variations in the velocity at the inlet to the gas turbine.

References

[1]Pearson, H., and McKenzie, A. B., "Wakes in Axial Compressors," *Journal of the Royal Aeronautical Society*, Vol. 63, July 1959, pp. 415, 416.

[2]Reid, C., "The Response of Axial Flow Compressors to Intake Flow Distortion," American Society of Mechanical Engineers Conf. and Products Show, Cleveland, OH, March 1969; also American Society of Mechanical Engineers 69-GT-29, 1969.

[3]Williams, D. D., "Review of Current Knowledge on Engine Response to Distorted Inflow Conditions," *AGARD Conference Proceedings Propulsion and Energetics 68th Annual Specialists Meeting* (Munich, Germany), 1986, pp. 1.1–1.32 (AGARD 400).

[4]Hynes, T. P., Chue, R., Greitzer, E. M., and Tan, C. S., "Calculations of Inlet Distortion Induced Compressor Flowfield Instability," *AGARD Conference Proceedings Propulsion and Energetics 68th Annual Specialists Meeting* (Munich, Germany), 1986, pp. 7.1–7.15 (AGARD 400).

[5]Biesiadny, T. J., Braithwaite, W. M., and Soeder, R. H., "Summary of Investigations of Engine Response to Distorted Inlet Conditions," *AGARD Conference Proceedings Propulsion and Energetics 68th Annual Specialists Meeting* (Munich, Germany), 1986, pp.15.1–15.21 (AGARD 400).

[6]"Aerospace Recommended Practice, ARP 1420," *Gas Turbine Engine Inlet Flow Distortion Guidelines*, Society of Automotive Engineers, March 1978.

[7]"Aerospace Information Report, AIR 1419," *Inlet Total-Pressure-Distortion Considerations for Gas Turbine Engines*, Society of Automotive Engineers, May 1983.

[8]Seddon, J., and Goldsmith, E. L., *Intake Aerodynamics*, William Collins and Sons Co., Ltd, London, 1985.

[9]*Turmo IVB Overhaul Manual*, Turbomeca, France, May 1987.

Static Aeroelastic Characteristics of a Composite Wing

In Lee* and Seung-Ho Kim†
Korea Advanced Institute of Science and Technology, Taejon, Republic of Korea
and
Hirokazu Miura‡
NASA Ames Research Center, Moffett Field, California 94035

Introduction

STATIC aeroelasticity is a problem involving the response of a flexible structure to aerodynamic loading and is a

Received Feb. 2, 1992; revision received Nov. 19, 1993; accepted for publication Jan. 11, 1994.

*Associate Professor, Department of Aerospace Engineering. Member AIAA.

†Graduate Research Assistant, Department of Aerospace Engineering.

‡Research Scientist. Member AIAA.

primary design parameter affecting structural optimization, vehicle aerodynamic stability, control effectiveness, and overall performance.[1] The analysis of static aeroelasticity requires the calculation of a static response including loads and stresses in the structure. Recent development in laminated composite materials enables the design of lighter aircraft structures that have sufficient strength and stiffness. Several studies have been performed for the static aeroelastic analysis of the composite wing.[2-4]

The objectives of this study are to investigate the effect of fiber orientation on the deformation pattern and the aerodynamic coefficients of the cantilevered composite wing. The wing structure is assumed as a plate-like wing. The finite element method for a laminated composite plate that accounts for the transverse shear deformation has been used for the structural analysis. The vortex lattice method[5] has been applied to the various-shaped thin wings for the aerodynamic analysis. The aerodynamic forces are interpolated to the structural nodal forces by the surface spline method.[6] The deformed shape of a wing and redistributed aerodynamic forces are obtained from an iteration procedure. Various-shaped thin wings are analyzed, and parametric studies for the sweep angle, the fiber orientation, and the freestream velocity are obtained to investigate the flexibility effect of the laminated composite wing.

Analysis

For the estimation of aerodynamic load, the wing is assumed to be a thin lifting surface flying in the low subsonic Mach number regime. Structurally, the wing is assumed as a thin plate and, initially, the aerodynamic forces on the undeformed wing are calculated by the linear vortex lattice panel method. These aerodynamic forces are interpolated to the finite element nodal forces. Thus, the deformed wing configuration is determined from the solution of the finite element equation. The aerodynamic forces on the deformed wing are again calculated and this iteration procedure is continued until the final deformation state is reached.

In this study, the independent variables for FEM analysis are the transverse displacement w, and two rotation angles ϕ_x and ϕ_y. The variables ϕ_x, ϕ_y, and w are approximated by the Lagrange interpolation functions ψ_i associated with the rectangular element

$$w = \sum_{i=1}^{n} w_i\psi_i, \qquad \phi_x = \sum_{i=1}^{n} \phi_x^i\psi_i, \qquad \phi_y = \sum_{i=1}^{n} \phi_y^i\psi_i \tag{1}$$

where n is the number of nodes, and ψ_i is the shape functions. For the case of 4-node isoparametric element, the shape functions are expressed in terms of natural coordinate ξ and η:

$$\begin{aligned} \psi_1 &= \tfrac{1}{4}(1-\xi)(1-\eta), & \psi_2 &= \tfrac{1}{4}(1+\xi)(1-\eta) \\ \psi_3 &= \tfrac{1}{4}(1+\xi)(1+\eta), & \psi_4 &= \tfrac{1}{4}(1-\xi)(1+\eta) \end{aligned} \tag{2}$$

With the use of Eq. (1), the finite element equation can be obtained as follows:

$$\begin{bmatrix} [K^{11}] & [K^{12}] & [K^{13}] \\ & [K^{22}] & [K^{23}] \\ \text{symmetric} & & [K^{33}] \end{bmatrix} \begin{Bmatrix} \{w\} \\ \{\phi_x\} \\ \{\phi_y\} \end{Bmatrix} = \begin{Bmatrix} \{F^1\} \\ \{F^2\} \\ \{F^3\} \end{Bmatrix} \tag{3}$$

The elements of the stiffness matrix $[K]$ are listed in Ref. 7. Here, the force vectors are obtained from the surface spline transformation of the aerodynamic forces that are calculated from the vortex lattice method.[5]

The grid system of the finite element method and the vortex lattice method do not necessarily coincide. The surface spline method[6] has been used to match the forces and the displacements of the two different grid systems.

The relation between FEM structural displacement $\{u_g\}$ and vortex lattice displacement $\{u_k\}$ is as follows:

$$\{u_k\} = [G_{kg}]\{u_g\} \tag{4}$$

where $[G_{kg}]$ is the interpolation matrix between two displacement sets.

The aerodynamic forces computed from the vortex lattice method are related to finite element nodal forces through

$$\{F_g\} = [G_{kg}]^T\{F_k\} \tag{5}$$

Results and Discussion

Three types of wings (sweep angle 0, 30, −30 deg) have been investigated to determine the influence of wing flexibility. Wing deformation was obtained for a right wing clamped at the wing root, however, the total wing was considered for calculation of aerodynamic forces since there is aerodynamic induction between the left and the right wing. The wing considered is constructed of T300/5208 Gr/Ep with the following material properties and size:

E_1	$= 20.0 \times 10^6$ psi
E_2	$= 1.40 \times 10^6$ psi
G_{12}	$= G_{13} = 0.8 \times 10^6$ psi
G_{23}	$= 0.6 \times 10^6$ psi
ν_{12}	$= 0.3$
half wing span	= 15 in.
chord	= 5 in.
taper ratio	= 0.6
ply thickness	$= 4.92 \times 10^{-3}$ in.

The stacking sequence is $[\theta_2/90_2]_s$, where θ is the fiber orientation angle measured from the line normal to midchord line, and the counterclockwise rotation is the positive fiber orientation angle. The sweep angle Λ is measured from the span axis to the midchord line.

The number of aerodynamic panels used is 200 (10 chordwise and 20 spanwise division) for the right wing. The number of finite elements used are 120 (8 chordwise and 15 spanwise division) for the right wing.

Effects of Fiber Orientation on Deformation Pattern

The deformed patterns for three types of wing are shown in Fig. 1. For the unswept wing, the wash-out deformation was determined near the fiber orientation of $\theta = 135$ deg. The wash-in deformation is determined for the other fiber orientation. For the 30-deg swept-back wing, wash-out is the general deformation pattern. However, wash-in is observed at $\theta = 90$ deg. The deformation pattern of a 30-deg swept-forward wing is also shown in Fig. 1, and wash-in occurs dominantly because the wing loading near the leading edge results in a larger twisting moment. When proper fiber orientation ($\theta = 135$ deg) is used, the wash-in deformation can be reduced.

Figure 2 shows the wingtip deflection for the three types of wing sweep angle and various fiber orientation. For the unswept wing smaller deflection can be observed at $\theta = 90 \sim 120$ deg, due to both the large bending stiffnesses and the effect of coupling stiffnesses. The tip deflection pattern of the swept-back wing and the swept-forward wing is similar to the tip deflection of the unswept wing; however, the geometry effect and the different aerodynamic loading give different deformation patterns. It is noticeable that the deflection for the three types of wing can be reduced in a favorable manner in the range $\theta = 80 \sim 100$ deg. For the prevention of divergence, it is recommended that the fiber orientation must be in the range $\theta = 80 \sim 120$ deg.

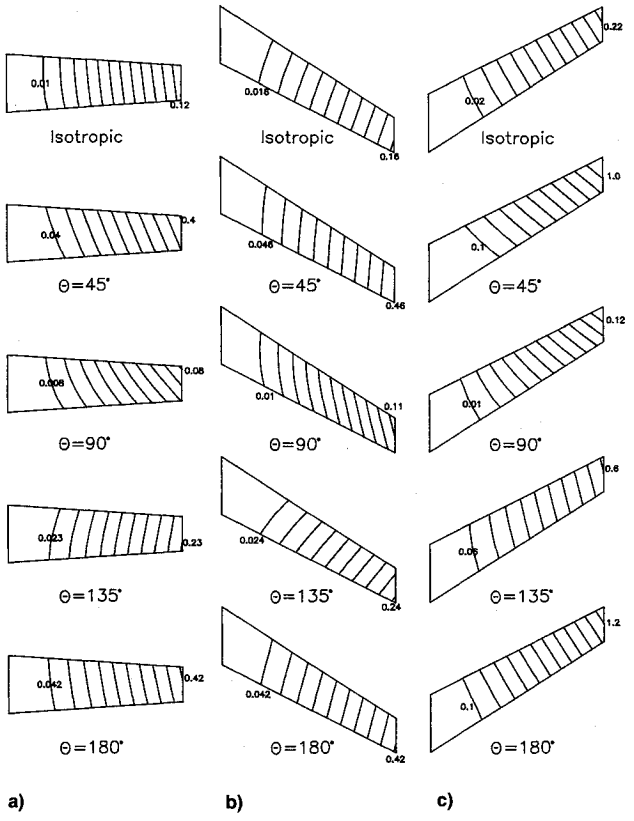

Fig. 1 Contour plot of deformed shape for $[\theta_2/90_2]_s$ wing models (U_∞ = 400 in./s, α = 2 deg, level unit = in.). Λ = a) 0, b) 30, and c) −30 deg.

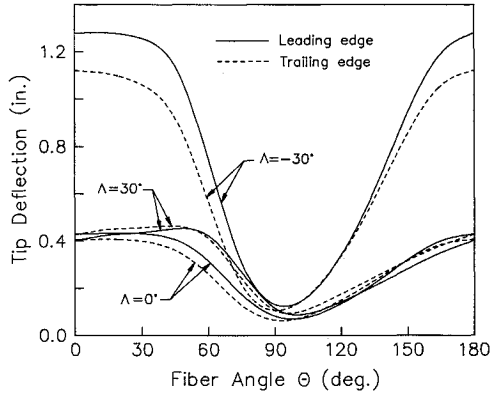

Fig. 2 Effect of fiber orientation θ upon tip deflections of $[\theta_2/90_2]_s$ wing models (U_∞ = 400 in./s, α = 2 deg).

Effects of Fiber Orientation on Aerodynamic Forces

The wing deformation is coupled with aerodynamic forces acting on the wing. The elastic effects on the total lift coefficients are examined for three wing sweeps. The results are shown in Fig. 3. For the unswept wing, large lift is developed at θ = 60 deg due to large wing deformation. When θ = 100 ~ 140 deg, lift coefficients are smaller than those of the rigid wing because of the wash-out effect. Larger lift forces are developed due to the wash-in deformation for the other fiber angles. The lift coefficients approach those of the rigid wing at angles θ = 100 and 140 deg. Although the deflection at θ = 140 deg is much larger than that of θ = 100 deg, the lift coefficient is almost the same because of the similar torsional deformation patterns. The significance of local angle-of-attack change is a result of torsional deformation. For the 30-deg swept-back wing, the lift coefficient at θ = 45 ~ 90 deg are larger than those of the rigid wing due to the wash-in deformation. For other fiber angles, smaller lift is observed due to the wash-out deformation, and lift coefficients are smaller than those of the rigid wing. For the swept-forward wing, larger lift coefficient is developed and the trend is similar to that of the unswept case. The lift coefficient of elastic wing approaches that of the rigid wing case at θ = 90 ~ 120 deg. For any fiber orientation, the lift is always larger than that of the rigid wing.

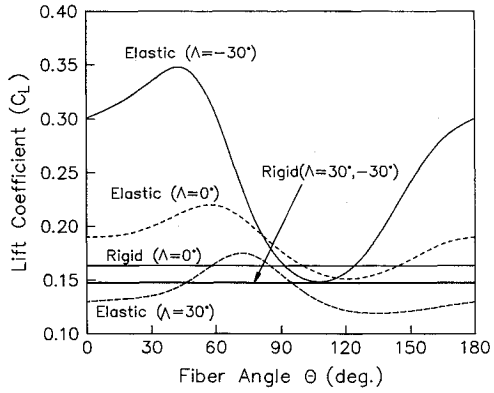

Fig. 3 Effect of fiber orientation θ upon lift coefficient of $[\theta_2/90_2]_s$ wing models (U_∞ = 400 in./s, α = 2 deg).

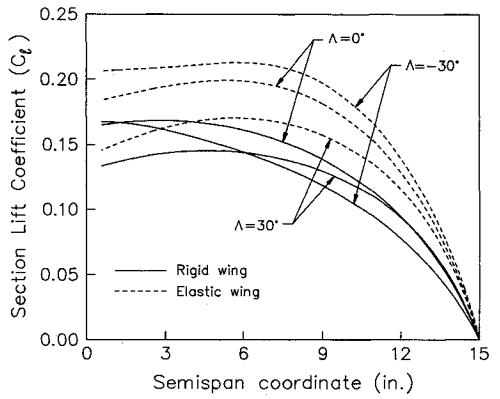

Fig. 4 Spanwise lift distribution of elastic and rigid wings ($[75_2/90_2]_s$, U_∞ = 400 in./s, α = 2 deg).

The spanwise lift variation for three wing sweep models are shown in Fig. 4. Wash-in cases (θ = 75 deg) are shown for three wing sweep model. Increase in spanwise lift distribution of elastic wings is observed for all cases. The highest increase in lift is obtained for the swept-forward wing, and the lowest increase is determined for the swept-back wing.

Conclusions

Three types of composite plate wings (sweep angle 0, 30, −30 deg) were analyzed to determine the deformation of cantilevered composite wings by the finite element method and aerodynamic loading by the vortex lattice method. T300/5208 Gr/Ep composite material of stacking sequence $[\theta_2/90_2]_s$ was used. The effect of fiber orientation and sweep angle on the deformation pattern of a wing and aerodynamic load changes was examined. The deformation patterns are affected by the fiber orientation. The typical deformation pattern of the unswept wing is wash-in, and the wash-out deformation is only observed at θ = 100 ~ 140 deg. The typical deformation pattern of the swept-back wing is wash-out, and the wash-in deformation is only observed at θ = 50 ~ 90 deg. The typical deformation pattern of the swept-forward wing is wash-in, and a small wash-out deformation is observed at θ = 105 deg. The optimum wing deformation for all three wings can be obtained at the fiber angle of θ = 90 ~ 120 deg.

References

[1]Wilson, E. G., "Static Aeroelasticity in the Design of Modern Fighters," *Static Aeroelasticity in Combat Aircraft*, AGARD Rept. 725, Jan. 1986.

[2]Bohlmann, J. D., Eckstrom, C. V., and Weisshar, T. A., "Static Aeroelastic Tailoring for Oblique Wing Lateral Trim," *Journal of Aircraft*, Vol. 27, No. 6, 1990, pp. 558–563.

[3]Librescu, L., and Thangjitham, S., "Analytical Studies on Static Aeroelastic Behavior of Forward-Swept Composite Wing Structures," *Journal of Aircraft*, Vol. 28, No. 2, 1991, pp. 151–157.

[4]Landsberger, B. J., and Dugundji, J., "Experimental Aero-Elastic Behavior of Unswept and Forward-Swept Cantilever Graphite/Epoxy Wings," *Journal of Aircraft*, Vol. 22, No. 8, 1985, pp. 679–686.

[5]Bertin, J. J., and Smith, M. L., *Aerodynamics for Engineers*, Prentice-Hall, Englewood Cliffs, NJ, 1979.

[6]Harder, R. L., and Desmarais, R. N., "Interpolation Using Surface Splines," *Journal of Aircraft*, Vol. 9, No. 2, 1972, pp. 189–191.

[7]Lee, I., Kim, S, Hong, C., and Miura, H., "Static Aeroelastic Analysis of Composite Wing," *Proceedings of the 17th International Council of the Aeronautical Sciences* (Stockholm, Sweden), 1990, pp. 594–601.

Experiments on the Automatic Control of Boundary-Layer Transition

J.-L. Rioual,* P. A. Nelson,† and M. J. Fisher‡
University of Southampton, Highfield, Southampton S017 1BJ, England, United Kingdom

Introduction

THE prospect of substantial savings in fuel costs has led to renewed interest in the subject of laminar flow control.[1,2] In particular, much attention has been devoted recently to the use of suction for the maintenance of laminar flow, since electron-beam drilled titanium sheet can now provide a sufficiently rigid and smooth porous surface through which fluid can be withdrawn. The use of suction itself consumes power, and it is important that the correct suction flow rate be applied for a given flow condition if the total net effective drag of a body is to be minimized. One way to monitor the effect of suction on a boundary layer is to monitor the position of transition. For a given flow condition (mean flow speed, turbulence level, pressure gradient), a desired transition position can be specified that will ensure the minimization of total net effective drag. In this brief Note we demonstrate that it is a simple matter to use measurements of the pressure fluctuations in the transition region of a flat plate boundary layer in order to define the actual position of transition. Furthermore, we demonstrate that the difference between the actual and desired values of transition position can be used to define an "error signal" for use in an automatic control loop that regulates the position of transition about its desired value.

Presented as Paper 92-02-010 at the DGLR/AIAA 14th Aeroacoustics Conference, Aachen, Germany, May 11–15, 1992; received Sept. 23, 1993; revision received Feb. 18, 1994; accepted for publication Feb. 18, 1994.

*Research Assistant, Fluid Dynamics and Acoustics Group, Institute of Sound and Vibration Research.

†Professor, Fluid Dynamics and Acoustics Group, Institute of Sound and Vibration Research.

‡Rolls Royce Reader, Fluid Dynamics and Acoustics Group, Institute of Sound and Vibration Research.

Experimental Apparatus

The experiments described in this Note were performed in a small wind tunnel having a 0.305- × 0.230-m working section of 2.5 m length, in which a 1.52-m-long plate was positioned. The tunnel allows mean flow velocities up to 22 ms^{-1}, hence, a Reynolds number based on the plate length of $Re_L = 2.2 \times 10^6$, with a turbulence level of 1%. The design of the rig for experimental investigation of boundary-layer suction is based upon the work reported by Reynolds and Saric.[3] The plate is made of a 1.2-m-long × 0.23-m-wide aluminium honeycomb core with 1.2-mm-thick aluminium skins, to which a carefully machined wooden leading edge was bonded, having a ratio of large to small axis of 35:1. Prior to the installation of the suction panel, an experiment consisting of traversing a hot wire probe just above the surface of the plate has shown that transition naturally occurs at $x_t = 0.65$ m downstream of the leading edge for a mean flow speed $U_0 = 20$ ms^{-1}, and at $x_t = 0.70$ m for $U_0 = 15$ ms^{-1}. The early onset of transition can be explained by the very high freestream turbulence level.[4] A suction panel was designed to allow suction from 0.46 m down to 0.645 m downstream of the leading edge, which corresponds to the first onset of transition for $U_0 = 20$ ms^{-1}. This suction panel was made of nine 16-mm (wide in flow direction) individual suction strips, each separated by 4 mm. A laser-drilled titanium sheet with holes of 0.1 mm in diam, randomly spaced by 1 mm, was carefully bonded to the suction panel. The aluminium plate was then drilled and machined in order to receive the suction panel with precision. A sketch of the plate with the suction panel is given in Fig. 1. Outside the wind tunnel, the nine pipes coming out of the suction panel were connected to a manifold, which was in turn connected to a fan. The fan was controlled by a PC via an inverter. Pressure fluctuation measurements were made downstream of the suction panel by using an array of electret microphones mounted flush with the plate surface. The microphone signals were conditioned, then acquired by the PC, which also controls the fan applying the suction. A sketch of all the equipment used is shown in Fig. 2.

Use of Pressure Fluctuations for Transition Control

The signals from the microphones were high-pass filtered above 800 Hz in order to remove the noise from the wind-tunnel fan. The PC illustrated in Fig. 2 enabled the signals to be sampled at a rate of 4 kHz. Some typical time histories are illustrated in Fig. 3. These results show clearly the development of the boundary layer from a laminar state to a

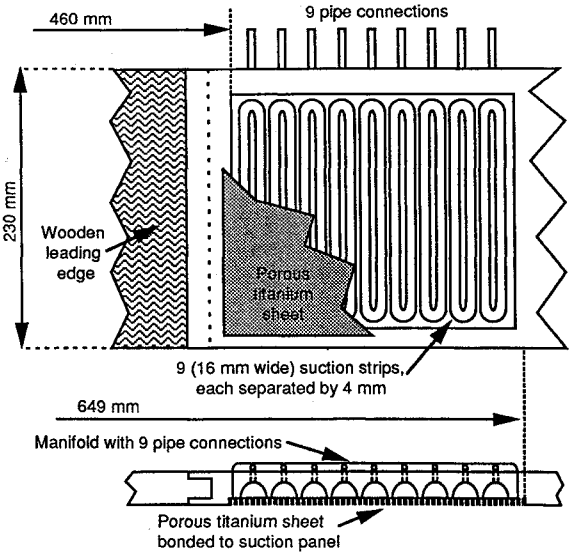

Fig. 1 Sketch of suction panel mounted on the plate.